International Journal of Environmental Sciences & Natural Resources
ISSN: 2572-1119

Juniper Publishers
key to the Researchers

Research Article
Volume 23 Issue 3 - February 2020
DOI: 10.19080/IJESNR.2020.23.556114

Int J Environ Sci Nat Res

Evaluating the GPR Method for Internal Drainage Diagnosis in Cranberry Fields

Jonathan A Lafond[1]*, Silvio J Gumiere[1], Awa Mbodj[1], Jacques Gallichand[1] and J Christian Dupuis[2]

[1]*Department of Soils and Agri-Food Engineering, Laval University, Canada*

[2]*Department of Geology and Geological Engineering, Laval University, Canada*

Submission: January 23, 2019; **Published:** February 05, 2020

***Corresponding author:** Jonathan A Lafond, Department of Soils and Agri-Food Engineering, Laval University, 2425, rue de l' Agriculture, Quebec City, G1V 0A6, QC, Canada

Abstract

Topsoil and subsoil compaction decreased soil drainage capacity and potentially increased runoff, leading to more soil erosion and contaminant transport from agricultural fields to the environment. A cost-effective, non-destructive, large scale method to identify problematic drainage areas would be of practical interest for growers. The objective of this study was to investigate and characterize spatial heterogeneity of soil hydraulic properties at the field scale using GPR measurements. GPR data were acquired at two cranberry fields: one made of organic soil and the other one, of mineral soil. Three-dimensional visualization of the field's stratification was possible after facies analyses and interpolation. Spatial variability of crop yield and saturated hydraulic conductivity of the fields were compared to GPR data by three different methods: means error calculation, entropy estimation and normalized map classes based on semi-variogram comparison. Data visualization combined with data analysis helped to highlight the geometry of the subsurface and important discontinuities. The results show that there is good correlation between areas where restrictive layers are closer to the surface and lower production yield. GPR data from both sites were found to have the highest similarity with crop yield data. The similarity level of the saturated hydraulic conductivity confirms the location of the restrictive layer

Keywords: Soil compaction; Hydraulic properties; Spatial heterogeneity; Ground penetrating radar; Soil stratification

Introduction

Improving efficiently the drainage of a field requires a good understanding of the spatial variability of the soil hydrodynamic properties [1-3]. Locating restrictive drainage layers, and mapping their extent, is of fundamental importance for optimizing drainage in cranberry fields. There are several techniques to characterize spatial variability of the soil properties. The most appropriate technique depends on the spatial scale of interest. At the small scale, the capacitive sensor method, such as pressure probes, provides information on the water table level in the soil [4]. Pressure probe measurements can be combined with tensiometer measurements to monitor the relationship between water table elevation and the soil matric potential. Gumiere et al. [2] used a combination of tensiometers and water table level sensors to characterize field drainage problems related to the spatial variability of soil properties. Other techniques, including time-domain reflectometry (TDR) and soil core sampling [4], have been used to characterize soil water spatial variability and drainage issues. The TDR method is well adapted to measure soil water content at a high temporal resolution; however, measurements are spatially limited to locations where the probes are installed [5]. Hydraulic properties of the soil can also be measured by various field infiltration tests: the auger hole method [6], infiltrometer tests [7] and pumping tests [8]. Sampling and laboratory analysis allow soil parameters, such as water content, particle size distribution, water retention curve and hydraulic conductivity to be determined [2,9]. These point-specific measurements are, however, destructive, very limited spatially, and are time consuming for mapping the variability of soil hydraulic properties over large areas. These measurements could also disturb the soil structure and induce errors [10].

At the field scale, characterizing hydrogeological variability with sufficient accuracy is of the utmost importance for water management. Geophysical methods seem to be applicable at this scale. Electrical resistivity tomography has been widely used to differentiate subsurface features by imaging electrical resistivity changes [11-13]. Electrical resistivity is related to soil water content and, therefore, can be used to indirectly monitor water or tracer infiltration [12,14-16]. Electrical resistivity requires a

close contact between the electrodes and the soil, which can be a problem when evaluating perennial cultures such as cranberries, because of the destructive effect of the probes on plants and fruits.

Ground-penetrating radar (GPR) is a promising alternative to electrical resistivity because its response is also affected by the soil water content [4,5,10]. GPR is a non-invasive geophysical method which can provide resolution in the order of the centimeter. The basis of this method is the propagation of electromagnetic waves within the soil. The velocity of propagation of these waves and their reflections at boundaries are governed by the dielectric permittivity of the soil and its conductivity, both of these affected by the soil water content [4]. As dielectric permittivity is strongly influenced by soil water content, it is possible to correlate the observed wave velocities with soil water content [5]. Daniels [17] showed that the attenuation of the electromagnetic energy, and of the corresponding permittivity, can be interpreted from relationships with soil texture and, therefore, makes it possible to identify horizons of the soil profile. In the unsaturated zone of the soil profile, GPR was successfully used to estimate soil water content [18], to follow the wetting front [19] and the migration of pollutants [20], and to identify the soil hydraulic properties such as saturated hydraulic conductivity, bulk density and field capacity [21,22]. The GPR has also been used to investigate stratigraphy and to locate groundwater [23].

In cranberry farms, soil stratigraphy has been successfully mapped through the interpretation of GPR images in order to characterize the field subsurface topography [24,25]. Despite these early successes, the use of GPR in cranberry's culture is still poorly documented, as is the relationships between subsoil characteristics, GPR measurements and soil hydrodynamic properties [26]. The few previous GPR studies are for cranberries growing in organic (muck) soils; but presently, modern cranberry beds are mostly constructed with sand over mineral soil. The drainage characteristics of these two types of substrates (organic and mineral) are different and their related drainage problems are therefore distinct.

The purpose of this study was

a) to investigate the location of restrictive drainage layers and characterize their extents in cranberry fields using ground penetrating radar imaging, and

b) to compare the data obtained from ground penetrating radar with crop yields and saturated hydraulic conductivities measured by conventional methods.

Materials and Methods

Study area

Two cranberry fields in the Quebec province (Canada) were selected. The first one (Site A) is located at 48°49' N 71°52' W, in the north of the Lac St-Jean region, and the second one (Site B) is at 46°16' N 71°58' W, in the main Quebec cranberry production basin. The construction of the cranberry beds consists in excavating the original soil material and backfilling with a uniform sand layer of 20 to 30cm. As shown in Table 1, Site A was built on an organic (muck) soil deposit and Site B, on a mineral soil deposit.

Table 1: Subsoil description of study sites [42].

		Site A	Site B
Basement Geology	Geological province	Grenville province	Appalaches province
	Lithologic name	Anorthositic suite of Lac-Saint-Jean	Formation of Saint-Anselme mountain (Saint-Roch Group)
	Geological zone description	Anorthosite, leuconorite, gabbro, norite and ultramafic rocks	Mafic volcanic rocks, alkaline basalt in massive stream
Quaternary Geology	Lithologic structure	Stratification	Stratification
	Deposit type	Undifferentiated organic sediment	Eolian, glaciomarine littoral and pre-littoral, deltaic, fluvioglacial
	Primary lithofacies	-	Fine sand, medium sand
	Secondary lithofacies	-	At oblique stratification in trough

The cranberry field was 45m wide by 360m long at Site A, and 45m wide by 460m long at Site B. Both fields were surrounded by shallow ditches, then 5m wide embankments. The ditches are regularly cleared of vegetation and sediments to promote efficient surface drainage [27]. Drainage system was also part of each site and consisted in 3 drains (15 meters apart) installed parallel to the length of the field at a depth between 0.6 and 0.9m, and either connected to a collector or directly to a deeper ditch after the embankment. Both fields were planted with *Vaccinium macrocarpon* Ait. (Stevens cultivar), which produces large berries and has a high root growth potential. Cranberry is a perennial plant; both fields had been under production for more than 30 years.

Water is involved at all stages of the cranberry production. For winter dormancy, the fields are flooded to form a protective ice layer over the seedlings. In spring, during the vegetative growth, protection against night frost is provided by irrigation. During summer, irrigation is used to supply plant evapotranspiration needs. During fall, the beds are flooded under 0.2-0.4m of water causing ripe cranberries to float at the surface, after which they

How to cite this article: Lafond, Gumiere, Mbodj, Gallichand, Dupuis. Evaluating the GPR Method for Internal Drainage Diagnosis in Cranberry Fields. Int J Environ Sci Nat Res. 2020; 23(3): 555614. DOI: 10.19080/IJESNR.2020.23.556114

are harvested by pumping. Water management is performed in a semi-closed water system where water used for irrigation is stored after drainage. Permanent networks of sprinklers connected to pumps can provide a water application rate of 4mm/h for irrigation.

Ground penetrating radar surveys

The GPR system was a SIR 3000 (Geophysical Survey Systems Inc. (GSSI), Nashua, NH, USA). A GSSI shield antenna of 270MHz, which is configured in a monostatic mode (the transmitter and receiver are in the same enclosure), was used. The antenna was also equipped with a trundle wheel for distance measurements. Measurements were made on a set of parallel transects, spaced 7m apart. A GPS-RTK (Viva GS08, Leica Geosystems) was used for geo-referencing the transects. Transects were made perpendicularly to the length of the field, with 49 transects at Site A and 57 transects at Site B.

The depth of investigation and the resolution depend on the frequency of the antenna and the attenuation caused by conductive and dielectric losses in the soil. Higher frequency antennas provide higher resolution, but at the expense of investigated depth [28]. At both sites, the best compromise between resolution and depth of investigation was obtained with the 270 MHz antenna, allowing the signal to reach a depth between 5 and 6m. This was sufficient to detect the primary sedimentary structures (e.g. deposit layers, angle of deposits, etc.) while keeping the centimeter vertical resolution.

In order to increase wave penetration and to reduce noise, all GPR measurements were performed in the winter of 2014, when the water table was at its lowest. As mentioned, growers flooded when it is cold enough in order to make an ice layer that will protects the plants, but once it is done, they lowered the water table as much as possible, *i.e.* around 1.5m depth. Thus, each site was covered in ice and snow. The two-way wave travel times were converted into depth by using a velocity matching model based on reflection hyperbolas observed from known target, such as irrigation pipes. The estimated wave velocities varied from 0.15 to 0.29m/ns, with an average of 0.206 m/ns. This velocity was used to convert the vertical time scale of the radargrams into a depth scale according to equations 1 and 2:

$$v = \frac{c}{\sqrt{\varepsilon}} \quad (1)$$

where v is the speed of the electromagnetic wave (m/s), is the speed of light (3×10^8m/s), and ε is the relative dielectric permittivity;

$$d = \frac{t \times v}{2} \quad (2)$$

where d is the depth (m) and t is the two-way travel time (s). Along the profiles, a GPR trace was acquired at every 0.2m and each trace had a length of 2048 samples.

Dynamic penetrometer surveys

A lightweight dynamic penetrometer (Controls Group USA, Inc., Elgin, IL, USA) was used to evaluate soil penetration resistance (R_s in Newton) according to penetration depth (P_d in meters):

$$R_s = \frac{W_s}{P_d} \quad (3)$$

[29]

where W_s is the work done by the soil (J) which is directly link to the kinetic energy of the hammer (weight = 10kg and fall = 50cm).

We performed 2 surveys at site A and 2 surveys at site B, located about the middle of the first and last thirds of each field length, until a depth of 3 meters each time in order to corroborate the layers detected by the GPR. Effectively, the soil penetration resistance is a robust and precise indicator of the depth and thickness of more compacted layer which should be detected by the GPR.

Soil sampling

For comparison with GPR measurements, hydraulic conductivity at saturation (Ksat) was measured on a regular grid of 55 georeferenced points at each site. For each point, intact soil cores (6 cm diameter by 6 cm height) were sampled at the depths of 7.5cm and 22.5cm [30]. The soil cores were saturated from the bottom over a period of 24 hours. The Ksat was determined by the vertical constant head method of Reynolds & Elrick [31]. The nomenclature 'Ksat_7' and 'Ksat_22' refers to Ksat at 7.5 and 22.5cm depth, respectively. At each site and for each of the 55 points, crop yield was also evaluated over an area of 0.09m^2. The total quantity of fruits for each area was collected and weighted in the laboratory.

GPR image processing

Primary image processing was done with RADAN 7 [28]. Processing was used to reduce noise and improve the interpretability of readings. All GPR profiles presented in this study were treated according to the following processing sequence:

a) **Static correction (time-zero),** to determine the first important arrival and adjust the starting position of the time axis at this point. It is used to remove the layer of snow and vegetation;

b) **Finite-duration impulse response filter,** to remove unwanted low and high frequency noises. The upper and lower frequencies were customized depending on the noise present on each radargram. A background removal was added to eliminate low frequency noise bands;

c) **Gain,** to amplify the signal amplitudes by using a combination of spherical and exponential functions. Amplification was done to compensate any dissipation of energy during propagation in the soil and to match the dynamic range of the data to the visualisation system;

How to cite this article: Lafond, Gumiere, Mbodj, Gallichand, Dupuis. Evaluating the GPR Method for Internal Drainage Diagnosis in Cranberry Fields. Int J Environ Sci Nat Res. 2020; 23(3): 555614. DOI: 10.19080/IJESNR.2020.23.556114

Three-dimensional visualization was made possible using OpendTect [32], an open source seismic data interpretation tool also applicable to GPR data.

Facies setting and stratigraphy

Like most imaging techniques, the resulting scan is not a direct replica of the reality, but a representation of it. The radargram does not represent a section through the ground, but a pseudo-section which must be interpreted [33]. The different strata of a profile can be identified through the type of reflectors that are diagnosed for a change of environment. The differentiation between the subsoil units and their interpretations was made according to the method of Neal [34] that distinguishes the geometry of reflectors, their external 3D shapes and the actual facies. We used the facies terminology proposed by Neal [34]. This terminology describes four types of configuration: the shape of reflections, their dip, the relation between reflections, and the continuity of reflectors.

Maps comparison

Difference maps and similarity

From the description of the facies appearing on the radargrams, a three-dimensional map was obtained from all transects of each site to highlight the surfaces of strata through the profiles. The interpolation between transects was made by a mesh algorithm. The inverse distance weighting method was used as it is fast and easy to calculate, given the large number of data points (about 40 000 points). Interpolation of Ksat_7, Ksat_22 and yield data was performed using the Thin Plate Spline (TPS) method of the fields package in R [35-36].

From the resulting maps, a visual comparison can be made but observer bias could influence the maps interpretation [37]. An objective assessment of the similarity between the GPR maps and those of Ksat_7, Ksat_22 and Yield, was obtained from Equation 4, which gives the absolute difference for each cell of the two rasterized maps.

$$Difference = |data_{GPR} - data_i| \quad (4)$$

where $data_{GPR}$ is the normalized [0,1] GPR data, $data_i$ is the normalized [0,1] data where is either Yield, Ksat_7 or Ksat_22.

The difference maps were classified by a range of differences into 3 classes: Class 1 ∈ [0.5,1], Class 2 ∈ [0.2,0.5[, Class 3 ∈ [0,0.2[. On each map, the number of cells composing each class was used to calculate the percentage of the field surface area occupied by each class. Considering that a difference of 1 represents no similarity and, 0 a complete similarity, the similarity map was calculated by subtracting the average difference for all the cells between two maps.

Entropy

Shannon [38] introduced entropy to quantify the information present on a map:

$$H(x) = -\sum_{i=1}^{n} P_i \log_2 P_i \quad (5)$$

where $H(x)$ is the entropy of a discrete random variable *x*, *n* is the number of possible values of *x*, and P_i is the probability mass function.

For image analysis, entropy is measured using the distribution of pixels values of an image. The probability distribution can be estimated by counting the number of times each value occurs in the image and dividing it by the total number of occurrences. The entropy is not affected by the image size or values distribution but by the frequency of each value. An image consisting mostly of a single intensity will have low entropy, i.e. low information content. A high entropy value corresponds to an image with many different intensities, i.e. high information content. Similar entropy values correspond to similar dispersion of the probability distributions. Shannon's entropy was used to compare the average information content of the GPR, Yield, Ksat_7 and Ksat_22 maps.

Results and Discussion

Site A – organic soil

Facies and stratigraphy

Using the terminology of Neal [34], five main facies have been described (Table 2).

Figure 1: Soil profile at site A showing the textural discontinuity between sand and organic soil at a depth between 21 and 28cm (photo by Y. Périard).

Facies *A-f1*: This facies presents laterally continuous reflectors that are parallel and consistent with the horizon below. This layer is shallow and, predominantly in the first 0.20m of soil, corresponds to a wave propagation time of 4ns. The horizon corresponds to the topsoil, and the sandy composition explains the average amplitude of reflections.

Facies *A-f2*: This facies presents planar reflector with lateral continuity. Reflectors are parallel and this facies is mainly pres-

How to cite this article: Lafond, Gumiere, Mbodj, Gallichand, Dupuis. Evaluating the GPR Method for Internal Drainage Diagnosis in Cranberry Fields. Int J Environ Sci Nat Res. 2020; 23(3): 555614. DOI: 10.19080/IJESNR.2020.23.556114

ent between 0.05 and 0.4m (1-8ns). This layer is interpreted as restrictive to flow and is present on almost the entire field, which is rich in iron as shown on soil profiles (Figure 1; see Périard et al. [39] for more details on this soil profile). Penetrometer surveys (Figure 2) also show a quick augmentation of soil resistance around 0.4m depth. These ferrous concretions are at the origin of the large-amplitude reflections of this facies.

Table 2: Facies description at Site A.

Code	GPR Profile	Internal Structure	Associated Energy	Interpreted Layer
A-f1	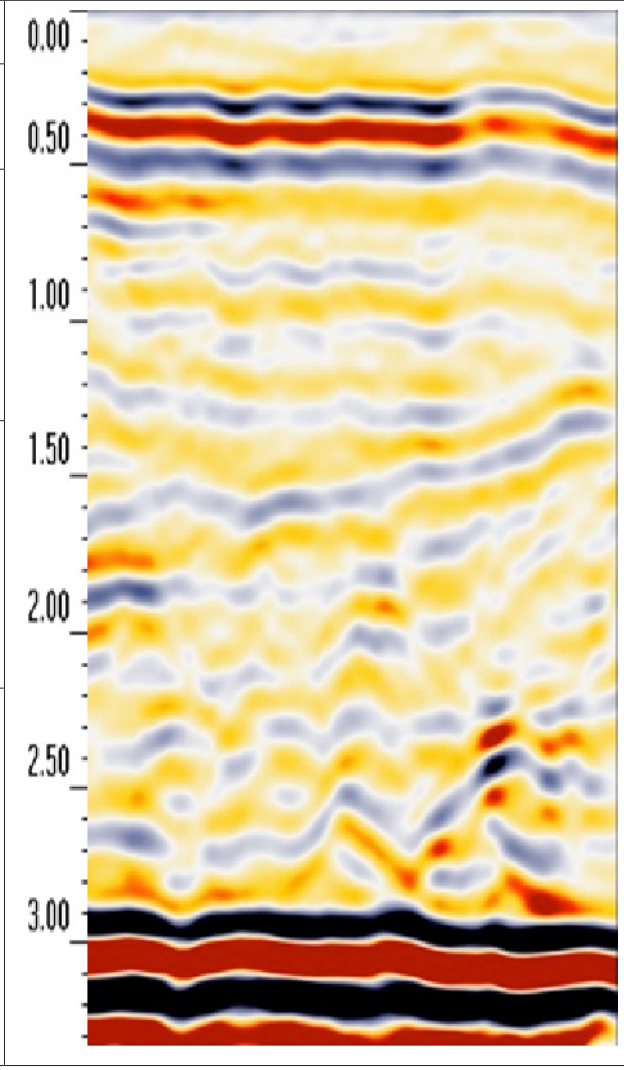		Average event energy	Topsoil layer
A-f2			High event energy	Iron rich restrictive horizon
A-f3			Average event energy	Sandy horizon
A-f4		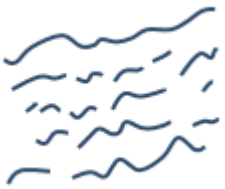		High water-content peat horizon
A-f5			Very high event energy	Saturated peat bed

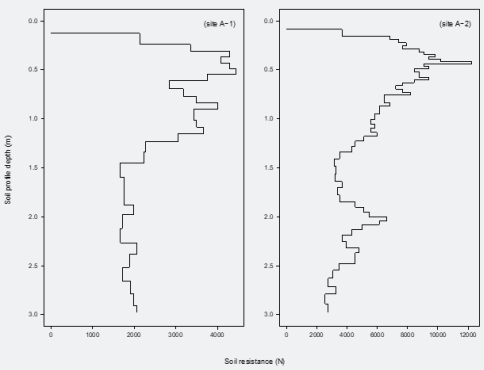

Figure 2: Soil resistance in function of depth in the soil profile calculated from the two dynamic penetrometer surveys (A-1 and A-2) realized at site A.

How to cite this article: Lafond, Gumiere, Mbodj, Gallichand, Dupuis. Evaluating the GPR Method for Internal Drainage Diagnosis in Cranberry Fields. Int J Environ Sci Nat Res. 2020; 23(3): 555614. DOI: 10.19080/IJESNR.2020.23.556114

Facies *A-f3*: Reflectors are laterally continuous, with a mild sinuosity, and consistent with the top layer. They are parallel, with occasional short and wavy reflectors. This layer is of highly variable thickness depending on the position in the field but can go down to 1.5m deep into the soil profile, underneath the drainage system. From this point around 1.5m depth, soil resistance has decreased and is almost constant until 3m depth (Figure 2), probably reflecting a high-water content or saturated peat soil (Facies *A-f4* and *A-f5*).

Facies *A-f4*: This facies is represented by a series of reflectors with limited lateral continuity. The reflectors are wavy with a complex geometry. They are sub-parallel with a moderate apparent dip. The energy associated with these reflectors is average, but slightly higher than for the previous layer. The interface between the two layers is planar and oblique and may represents the interface between the non-saturated and the underlying saturated peat.

Facies *A-f5*: Reflectors are laterally continuous and parallel to this facies. There may be a low to moderate dip depending on the position in the field. This layer is present on a portion of the field and its thickness is variable. It should represents the water table in the peat or may corresponds to the interface between saturated peat and the underlying mineral soil. Peat has a high saturated porosity that enhances the contrast of dielectric permittivity with the unsaturated peat layer above and, therefore, to the very large amplitude of reflections.

Five horizons have been determined through the analysis of facies: the topsoil, a restrictive layer, a sandy layer, an unsaturated peat layer and a saturated peat layer or a mineral layer. The restrictive layer is mainly caused by the iron upward/downward movement, oxidation and ferrous concretion between the topsoil and the sandy layer, before the underneath organic soil. This restrictive layer was observed by Périard et al. [39] at a depth between 0.12 and 0.49m below soil surface, depending on the location within site A. Effectively, observation of several profiles of soil through the field has confirmed the presence of this ferrous restrictive layer; one of the profiles is shown in Figure 1. The profiles and the restrictive layers of this field are discussed in Périard et al. [39] under Group 7. In summary, the vertical water movement in this soil is strongly limited. This restrictive layer does not seem to be related to the primary organic sedimentary structure of this geographical area. Diagenetic precipitation of iron oxide in unconsolidated sediment is related to the flow of interstitial water. Therefore, the flow path determines the nature and shape of precipitates [40]. In the case of cranberries, cultivation practices induce vertical water movement along the profile throughout the season. The cycle of water table elevation and drawdown leads to the precipitation of naturally occurring iron oxide in the organic material and may explain the continuous nature of this horizon throughout the entire field.

Mapping and comparison between soil properties and GPR

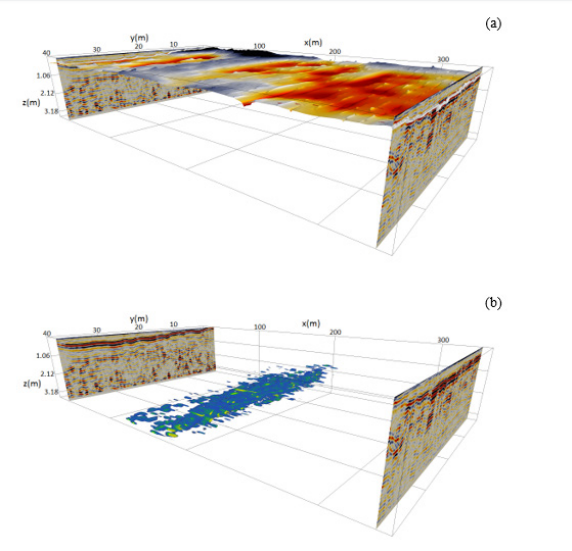

Figure 3: Three-dimensional maps at site A of (a) the restrictive layer, and (b) the peat bed (blue). Both images also show the first and last GPR transects of the field.

This restrictive layer is the most important underground drainage element of Site A; that is why we interpolated this layer only (Figure 3a). The reflectors of the peat bed (Figure 3b) do not appear to affect the configuration of the restrictive layer. The restrictive layer appears deeper, ranging from 0.4 to 0.8m, in some areas of the field, as shown in orange-red in Figure 3a. In other areas, the restrictive layer is closer to the surface, about 0.2 to 0.4m, as shown in dark-blue (Figure 3a). The restrictive layer at site A is

How to cite this article: Lafond, Gumiere, Mbodj, Gallichand, Dupuis. Evaluating the GPR Method for Internal Drainage Diagnosis in Cranberry Fields. Int J Environ Sci Nat Res. 2020; 23(3): 555614. DOI: 10.19080/IJESNR.2020.23.556114

deeper in the (x, y) area around (300m, 30m), whereas it is closer to the surface around (100m, 10m).

Figure 4 shows the maps of Ksat_7, Ksat_22, crop yield and GPR at site A. On the first look, both Ksat_7 (Figure 4a) and Ksat_22 (Figure 4b) do not match with the depth of the restrictive layer measured by GPR (Figure 4d), while crop yield (Figure 4c) and GPR (Figure 4d) seem to show similarities. Areas where the restrictive layer is deepest correspond to the most productive areas (orange in Figure 4c & 4d). Inversely, lowest yield areas correspond to shallower restrictive layer areas (blue color in upper left of the field). The main water-related problem that can influence crop yield is insufficient internal drainage and the nature of the restrictive layer. Peat soils have high porosity and a large water-holding capacity, but low hydraulic conductivity [41]. The deeper this restrictive layer, the more room the root system has to grow, therefore reducing the chances of suffering an hypoxic stress, and the more yield is likely to occur.

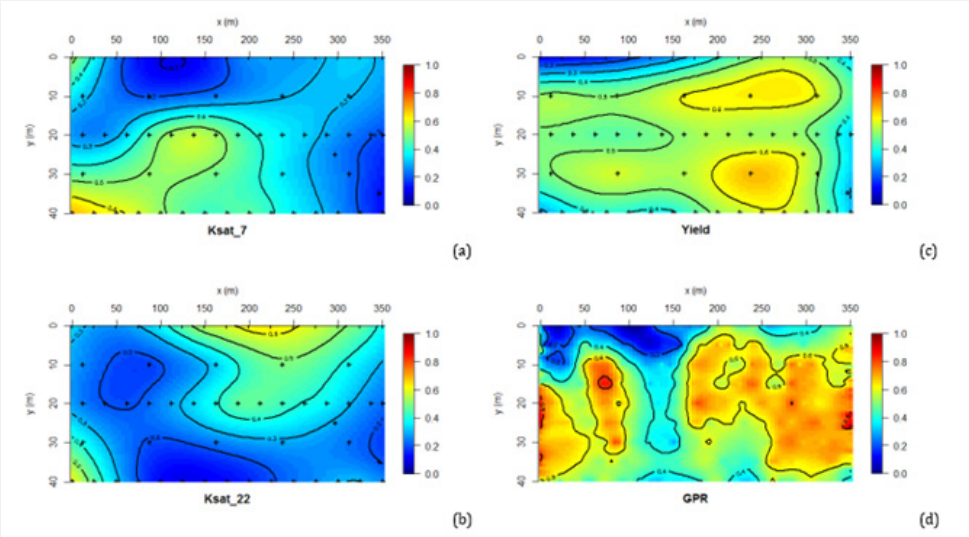

Figure 4: Normalized maps at site A for saturated hydraulic conductivity at 7cm (a) and at 22cm (b), crop yield (c), and depth of the restrictive layer measured by GPR (d).

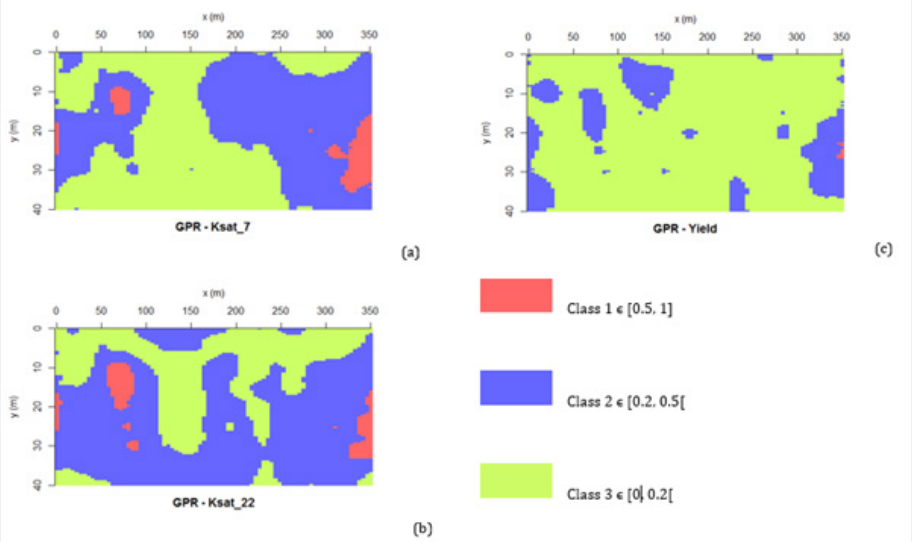

Figure 5: Maps of the difference at site A between the normalized GPR depth of the restrictive layer and normalized saturated hydraulic conductivity at 7cm (a) and 22cm (b) and crop yield (c).

Difference maps between GPR and Ksat_7, Ksat_22 and Yield are presented in Figure 5. Three classes of differences were defined. Yield is the variable which shows the least difference with GPR (Figure 5c) with an average difference of 0.12 (Class 3), compared to 0.23 (Class 2) for Ksat_7 (Figure 5a) and to 0.27 (Class 2) for Ksat_22 (Figure 5b). The similarity of GPR-Yield is 88% of

How to cite this article: Lafond, Gumiere, Mbodj, Gallichand, Dupuis. Evaluating the GPR Method for Internal Drainage Diagnosis in Cranberry Fields. Int J Environ Sci Nat Res. 2020; 23(3): 555614. DOI: 10.19080/IJESNR.2020.23.556114

the area against 77% for GPR-Ksat_7 and 73% for GPR-Ksat_22, which confirms the observations made from Figure 4. Shannon's entropy is 21.2 for GPR, 22.1 for Yield, 30.7 for Ksat_7 and 33.1 to Ksat_22. The entropy of Yield is much more similar to that of GPR than to those of Ksat_7 and Ksat_22, supporting the results of maps comparison.

Site B – mineral soil

Facies and stratigraphy

Similarly, to Site A, five main facies can be described using the terminology of Neal [34] and are presented in Table 3.

Table 3: Facies description at Site B.

Code	GPR Profile	Internal Structure	Associated Energy	Interpreted Layer
B-f1	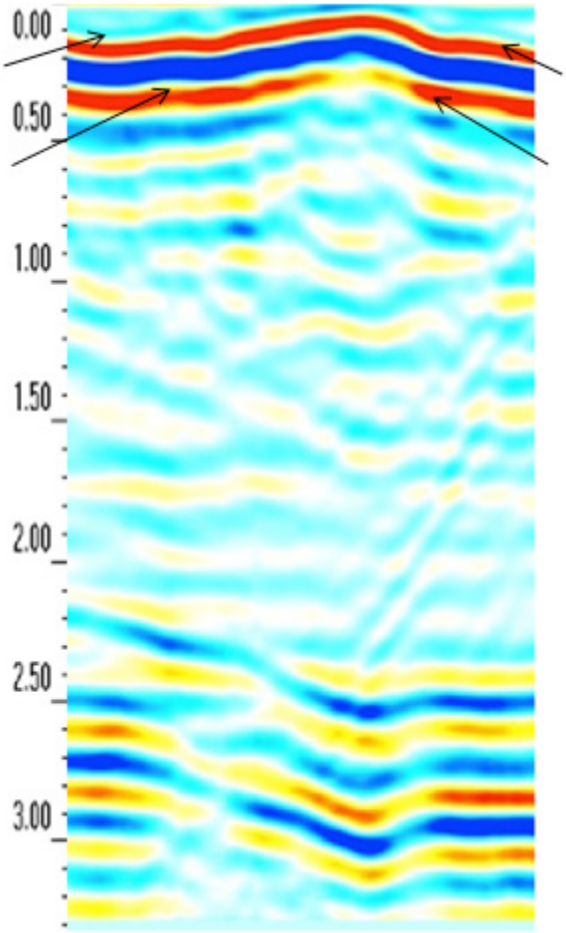		Average energy event	Sandy surface horizon
B-f2			Very high event energy	Partially restrictive horizon
B-f3			Average energy event	Sandy horizon
B-f4				High-water content mineral horizon
B-f5			High energy event	Original mineral deposit and/or water-table

Figure 6: Soil profile at site B showing the restrictive layer richer in iron at a depth between 8 and 23cm (photo by Y. Périard)

How to cite this article: Lafond, Gumiere, Mbodj, Gallichand, Dupuis. Evaluating the GPR Method for Internal Drainage Diagnosis in Cranberry Fields. Int J Environ Sci Nat Res. 2020; 23(3): 555614. DOI: 10.19080/IJESNR.2020.23.556114

Facies *B-f1*: This facies presents laterally continuous reflections which are parallel and consistent with the horizon below. This layer is shallow, predominantly in the first 0.20m of soil, and corresponds to a wave propagation time of 4ns. This horizon corresponds to the topsoil, and a sandy composition (Figure 6) may explain the average amplitude of reflections.

Facies *B-f2*: This facies presents planar and parallel reflections with a lateral continuity. The facies is mainly present between 0.05 and 0.5m (1 to 10ns). As for Site A, the interpreted layer can be restrictive to flow and seems to be present over the entire field. However, field observations (Figure 6; see Périard et al. [39] for more details on this soil profile) have pointed out that the soil profiles of this field are more uniform. Penetrometer surveys (Figure 7) also show a more gradual augmentation of soil resistance until around 0.4-0.5 meters depth. This layer can be the cause of the large-amplitude reflections of this facies.

Facies *B-f3*: It is represented by a series of reflections with a limited lateral continuity. The reflections are short and with a complex geometry (wavy or concave). Some have a low dip, but they are essentially horizontal. The energy associated with these reflectors is average and this horizon goes down to 1.7m (34ns), as we can also note by the penetrometer surveys (Figure 7, site B-1). The interface between the two layers is planar and horizontal; it represents the boundary between the saturated and sandy layers.

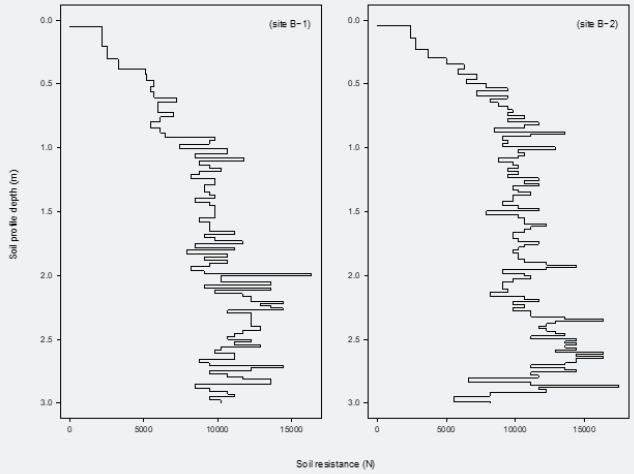

Figure 7: Soil resistance in function of depth in the soil profile calculated from the two dynamic penetrometer surveys (B-1 and B-2) realized at site B.

Facies *B-f4*: Reflectors are laterally continuous and parallel, with a low sinuosity. This layer has a highly variable depth according to the position in the field because it is dependent on the diagonal geometry of the next layer. The horizon corresponds to a high-water content mineral layer with average amplitude of reflectors.

Facies *B-f5*: Reflectors are continuous and parallel on this facies. They have a moderately marked dip from one longitudinal end of the field to the other. This facies corresponds either to the water-table and/or to the original geological deposit on which the sand was deposited. The change in soil horizon contributes to the contrast of dielectric constants with the layer above and increases the amplitude of reflections.

Five horizons have been determined through the analysis of facies: a topsoil, a restrictive layer, a sandy layer, a high-water content sandy layer and the water-table or original mineral deposit. Figure 6 shows the location of the restrictive layer through a soil profile from 8 to 23cm depth. The soil profiles of this field are discussed in Périard et al. [39] under Group 3. An overview of the water-table or original mineral deposit is shown in Figure 8a. The original deposit consists of remains of the Champlain Sea formed when the glaciers melted, leaving large quantities of sand [42]. The way in which the deposit was formed can explain marked differences in depth (Table 1).

Mapping and comparison between soil properties and GPR

In Figure 8, deeper areas are colored orange and red whereas shallower areas are colored dark blue, where we can see a shallow restrictive layer in the (x,y) area around (150m, 10m) of the field (Figure 8b). The shape and location of the original sand deposit appears to affect the configuration of the restrictive layer since there is a correspondence of location between the deeper and shallower areas of the two layers (Figure 8a & 8b).

Visual comparison of Ksat_22 and Yield maps with the GPR one seems to indicate that where the restrictive layer is the deeper, the larger are the values of Ksat_22 and Yield (Figure 9). At first look, maps of the restrictive layer measured by GPR (Figure 9d) and yield (Figure 9c) show similarities. As for Site A, the yield

How to cite this article: Lafond, Gumiere, Mbodj, Gallichand, Dupuis. Evaluating the GPR Method for Internal Drainage Diagnosis in Cranberry Fields. Int J Environ Sci Nat Res. 2020; 23(3): 555614. DOI: 10.19080/IJESNR.2020.23.556114

seems to be correlated to the depth of the restrictive layer (GPR), as the maximum yield values are located where the layer is deeper (orange in both figures). Inversely, yield is lower where the restrictive layer is shallower, around (x,y) of (150m, 10m).

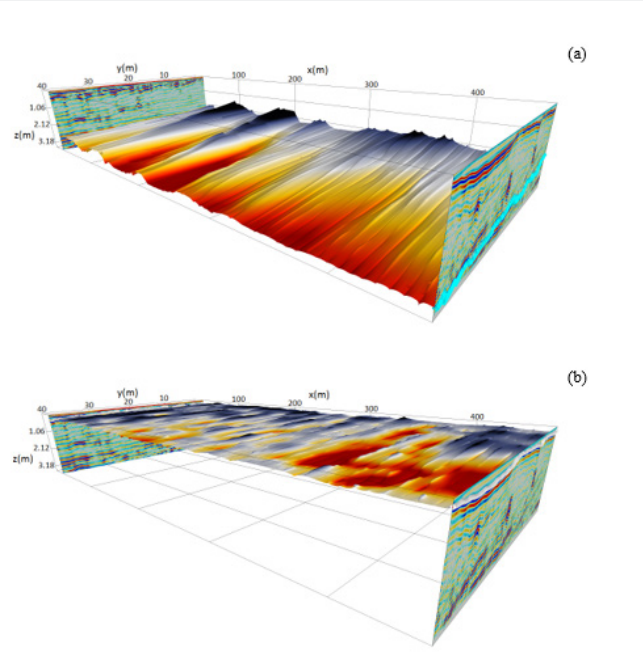

Figure 8: Three-dimensional maps at site B of (a) the water table layer, and (b) the restrictive layer. Both images also show the first and last GPR transects of the field.

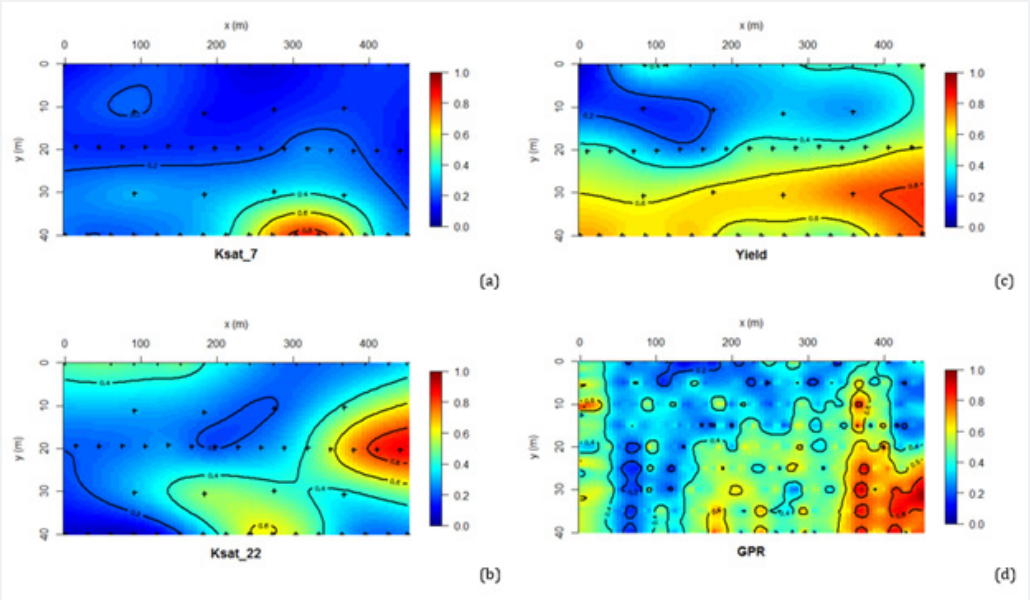

Figure 9: Normalized maps at site B for saturated hydraulic conductivity at 7cm (a) and at 22cm (b), crop yield (c), and depth of the restrictive layer measured by GPR (d).

Maps of the percentage difference between depth of the restrictive layer obtained by GPR, and Ksat_7, Ksat_22, and Yield are presented in Figure 10. The Yield and Ksat_22 have higher similarity with GPR, i.e. class 3 differences of 0.13 and 0.16 in average, respectively, compared to class 2 differences of 0.22 in average for Ksat_7. The corresponding similarity to GPR data is 87% for Yield, 84% for Ksat_22 and 78% for Ksat_7. These results support the visual observations made from Figure 9.

How to cite this article: Lafond, Gumiere, Mbodj, Gallichand, Dupuis. Evaluating the GPR Method for Internal Drainage Diagnosis in Cranberry Fields. Int J Environ Sci Nat Res. 2020; 23(3): 555614. DOI: 10.19080/IJESNR.2020.23.556114

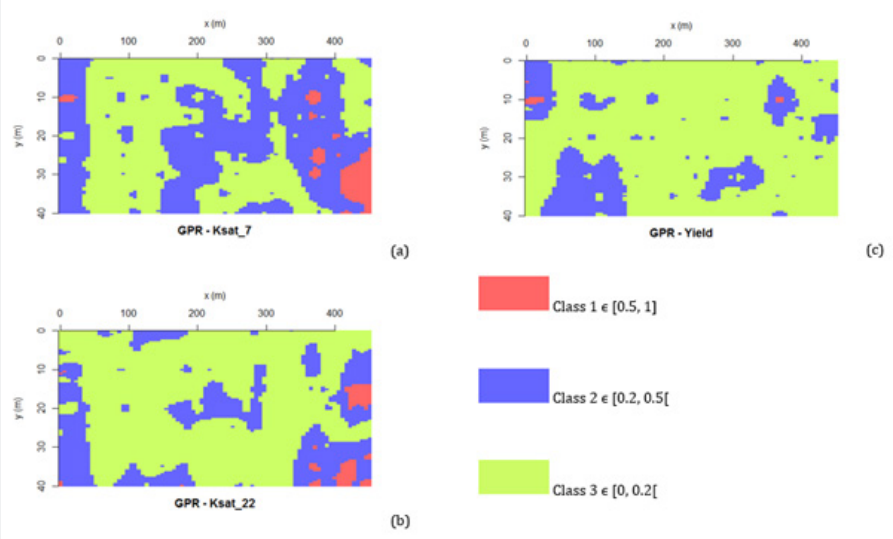

Figure 10: Maps of the difference at site B between the normalized GPR depth of the restrictive layer and normalized saturated hydraulic conductivity at 7cm (a) and 22cm (b) and crop yield (c).

Shannon's entropy is 24.2 for Yield, 43.5 for Ksat_7, 29.6 for Ksat_22 and 25.1 for GPR. The entropy of Ksat_22, Yield and GPR are almost equal, which confirms a certain homogeneity between the variables but cannot confirms the similarity between spatial patterns.

Conclusion

The subsurface topography of two cranberry fields (sites A and B) has been studied using stratigraphy and 3D visualization of ground penetrating radar (GPR) imaging. The differences between observed strata were highlighted through the analysis of five facies at both sites. This analysis allowed us to identify the main soil horizons including an anthropogenic and a geologic one. Data analysis and visualization helped to highlight areas of low saturated hydraulic conductivity. A restrictive hydraulic conductivity layer was located near the soil surface at each site using the GPR data. Areas where the restrictive layer was shallower also presented lower yields based on the strong similarity between GPR and Yield maps, then showing the influence of this restrictive layer location on cranberry yields. Three-dimensional mapping not only allowed to locate and determine the geometry of the discontinuities in the sub-surface of cranberry beds, but also to locate the most relevant areas for drainage and irrigation improvements in order to maximize yields.

Acknowledgement

The authors acknowledge the financial contribution of the Natural Sciences and Engineering Research Council of Canada (NSERC). They would also like to thank Hortau, Canneberges Bieler, Mont Atocas, Atocas Blandford, Pampev and Ferme Daniel Coutu for their financial and technical support. The data that support the findings of this study are available from the corresponding author upon reasonable request.

References

1. Bonin S (2009) Régie agroenvironnementale de l'irrigation dans la production de canneberges (*Vaccinium macrocarpon* Ait.). M. Sc. thesis, Université Laval, Québec, QC, p. 114.
2. Gumiere SJ, Lafond JA, Hallema DW, Périard Y, Caron J, et al. (2014) Mapping soil hydraulic conductivity and matric potential for water management of cranberry: Characterisation and spatial interpolation methods. Biosystems Eng 128: 29-40.
3. Pelletier V, Gallichand J, Gumiere S, Pepin S, Caron J (2015) Water table control for increasing yield and saving water in cranberry production. Sustainability 7(8): 10602-10619.
4. Weihermüller L, Huisman JA, Lambot S, Herbst M, Vereecken H (2007) Mapping the spatial variation of soil water content at the field scale with different ground penetrating radar techniques. J Hydrol 340(3): 205-216.
5. Huisman JA, Hubbard SS, Redman JD, Annan AP (2003) Measuring soil water content with ground penetrating radar. Vadose Zone J 2: 476-491.
6. Amoozegar A, Warrick AW (1986) Hydraulic Conductivity of Saturated Soils: Field Methods. American Society of Agronomy Part 1, Madison, WI, pp. 735-770.
7. Reynolds WD, Elrick DE (1991) Determination of hydraulic conductivity using a tension infiltrometer. Soil Sci Soc Am J 55(3): 633-639.
8. Neuman SP (1975) Analysis of pumping test data from anisotropic unconfined aquifers considering delayed gravity response. Water Resour. Res. 11(2): 329-342.
9. Gupta SC, Larson WE (1979) Estimating soil water retention characteristics from particle size distribution, organic matter content and bulk density. Water Resour Res 15(6): 1633-1635.
10. Lunt IA, Hubbard SS, Rubin Y (2005) Soil moisture content estimation using ground-penetrating radar reflection data. J Hydrol 307(1-4): 254-269.
11. Zhou W, Beck BF, Stephenson JB (2000) Reliability of dipole-dipole electrical resistivity tomography for defining depth to bedrock in covered karst terranes. Environ Geol 39(7): 760-766.

How to cite this article: Lafond, Gumiere, Mbodj, Gallichand, Dupuis. Evaluating the GPR Method for Internal Drainage Diagnosis in Cranberry Fields. Int J Environ Sci Nat Res. 2020; 23(3): 555614. DOI: 10.19080/IJESNR.2020.23.556114

12. Kemna A, Kulessa, B, Vereecken, H (2002) Imaging and characterisation of subsurface solute transport using electrical resistivity tomography (ERT) and equivalent transport models. J Hydrol 267(3): 125-146.

13. Maury SBS, Narshimulu G (2014) Ground water potential in fractured aquifers of Ophiolite formations, Port Blair, South Andaman Islands using electrical resistivity tomography (ERT) and vertical electrical sounding (VES). J Geological Sci India 83(4): 393-402.

14. Michot D, Benderitter Y, Dorigny A, Nicoullaud B, King D, et al. (2003) Spatial and temporal monitoring of soil water content with an irrigated corn crop cover using surface electrical resistivity tomography. Water Resour Res 39(5): 1138.

15. Vanderborght J, Kemna A, Hardelauf H, Vereecken H (2005) Potential of electrical resistivity tomography to infer aquifer transport characteristics from tracer studies: A synthetic case study. Water Resour Res 41(6).

16. Dietrich S, Weinzettel PA, Varni M (2014) Infiltration and drainage analysis in a heterogeneous soil by electrical resistivity tomography. Soil Sci Soc Am J 78(4): 1153-1167.

17. Daniels DJ (2004) Ground Penetrating Radar. (2nd edn), Volume 1. IET, p. 726.

18. Oden CP, Olhoeft GR, Wright DL, Powers MH (2008) Measuring the electrical properties of soil using a calibrated ground-coupled GPR System. Vadose Zone J 7(1): 171-183.

19. Saintenoy A, Schneider S, Tucholka P (2008) Evaluating ground penetrating radar use for water infiltration monitoring. Vadose Zone J 7(1): 207-214.

20. Cassidy NJ (2008) GPR attenuation and scattering in a mature hydrocarbon spill: A modeling study. Vadose Zone J 7(1): 140-159.

21. Jonard F, Weihermueller L, Schwank M, Jadoon KZ, Vereecken H, et al. (2015) Estimation of Hydraulic Properties of a Sandy Soil Using Ground-Based Active and Passive Microwave Remote Sensing. IEEE Trans Geosci Rem Sens 53(6): 3095-3109.

22. Lambot S, Slob E, Rhebergen J, Lopera O, Jadoon K, et al. (2009) Remote Estimation of the Hydraulic Properties of a Sand Using Full-Waveform Integrated Hydrogeophysical Inversion of Time-Lapse, Off-Ground GPR Data. Vadose Zone J 8(3): 743-754.

23. Mahmoudzadeh MR, Francés AP, Lubczynski M, Lambot S (2012) Using ground penetrating radar to investigate the water table depth in weathered granites - Sardon case study, Spain. J Applied Geophys 79: 17-26.

24. Turenne J (1993) Ground penetrating radar investigations on cranberry beds in Plymouth County, Massachusetts. In Proceedings of the Second Government Workshop on GPR: Technologies and Applications, pp. 213-220.

25. Turenne J (1997) Understanding cranberry soil maps. Cranberries 61: 15-18.

26. Turenne JD, Doolittle JA, Tunstead R (2006) Ground-penetrating radar and computer graphic techniques are used to map and inventory Histosols in southeastern Massachusetts. Soil Surv Horiz 47(1): 13-17.

27. DeMoranville CJ (2001) Reducing management costs in Cranberry production. Cranberry station fact sheet. Paper 13.

28. GSSI (Geophysical Survey Systems Inc.) (2016) RADAN software. Salem, NH, USA.

29. Herrick JE, Jones TL (2002) A dynamic cone penetrometer for measuring soil penetration resistance. Soil Sci Soc Am J 66: 1320-1324.

30. Blake GR, Hartge KH (1986) Bulk density. In: Klute A (Ed.), Methods of soil analysis, Part 1. Physical and Mineralogical methods. American Society of Agronomy, Madison, W, pp. 363-375.

31. Reynolds WD, Elrick DE (2002) Constant head soil core (tank) method. In: Dane JH, Topp GC (Eds.), Methods of soil analysis, Part 4. Physical methods. Soil Science Society of America, Madison, WI. Book Series No.5, pp. 804-808.

32. GB Earth Sciences (2016) OpendTect software. Enschede, The Netherlands.

33. Moorman B, Robinson S, Burgess M (2007) Imaging near-surface permafrost structure and characteristics with Ground-Penetrating Radar. CSEG Recorder J 32(2): 23-30.

34. Neal A (2004) Ground-penetrating radar and its use in sedimentology: Principles, problems and progress. Earth Sci Rev 66: 261-330.

35. Nychka D, Furrer R, Paige J, Sain S (2015) Fields: Tools for spatial data. R package version 9.0.

36. R Core Team (2016) R: A language and environment for statistical computing. R Foundation for Statistical Computing, Vienna, Austria.

37. Berry JK (1999) Comparing Maps by the Numbers. Beyond Mapping column, GEO World, September issue: 23-24.

38. Shannon CE (1948) A mathematical theory of communication. Bell System Tech J 27(3): 379-427.

39. Périard Y, Gumiere SJ, Rousseau AN, Caillier M, Gallichand J, et al. (2017) Assessment of the drainage capacity of cranberry fields: Problem identification using soil clustering and development of a new drainage criterion. Can J Soil Sci 97: 56-70.

40. Van Dam RL (2001) Causes of ground-penetrating radar reflections in sediment. Unpubl. PhD Thesis, Univ. Amsterdam. Amsterdam, The Netherlands, p. 110.

41. Kechavarzi C, Dawson Q, Leeds-Harrison PB (2010) Physical properties of low-lying agricultural peat soils in England. Geoderma 154(3-4): 196-202.

42. Ministère de l'Énergie et des Ressources Naturelles (MERN) (2015) SIGEOM.

How to cite this article: Lafond, Gumiere, Mbodj, Gallichand, Dupuis. Evaluating the GPR Method for Internal Drainage Diagnosis in Cranberry Fields. Int J Environ Sci Nat Res. 2020; 23(3): 555614. DOI: 10.19080/IJESNR.2020.23.556114

DOI: 10.19080/IJESNR.2020.23.556114

How to cite this article: Lafond, Gumiere, Mbodj, Gallichand, Dupuis. Evaluating the GPR Method for Internal Drainage Diagnosis in Cranberry Fields. Int J Environ Sci Nat Res. 2020; 23(3): 555614. DOI: 10.19080/IJESNR.2020.23.556114